Journal of Human Evolution 55 (2008) 682–690

Contents lists available at ScienceDirect

Journal of Human Evolution

journal homepage: www.elsevier.com/locate/jhevol

A quantitative method for the evaluation of three-dimensional structure of temporal bone pneumatization

Cheryl A. Hill*, Joan T. Richtsmeier

Department of Anthropology, The Pennsylvania State University, University Park, PA 16802, United States

ARTICLE INFO

Article history:
Received 8 August 2007
Accepted 27 March 2008

Keywords:
Computed tomography
Hominid
Olive baboon
African apes

ABSTRACT

Temporal bone pneumatization has been included in lists of characters used in phylogenetic analyses of human evolution. While studies suggest that the extent of pneumatization has decreased over the course of human evolution, little is known about the processes underlying these changes or their significance. In short, reasons for the observed reduction and the potential reorganization within pneumatized spaces are unknown. Technological limitations have limited previous analyses of pneumatization in extant and fossil species to qualitative observations of the extent of temporal bone pneumatization. In this paper, we introduce a novel application of quantitative methods developed for the study of trabecular bone to the analysis of pneumatized spaces of the temporal bone. This method utilizes high-resolution X-ray computed tomography (HRXCT) images and quantitative software to estimate three-dimensional parameters (bone volume fractions, anisotropy, and trabecular thickness) of bone structure within defined units of pneumatized spaces. We apply this approach in an analysis of temporal bones of diverse but related primate species, *Gorilla gorilla*, *Pan troglodytes*, *Homo sapiens*, and *Papio hamadryas anubis*, to illustrate the potential of these methods. In demonstrating the utility of these methods, we show that there are interspecific differences in the bone structure of pneumatized spaces, perhaps reflecting changes in the localized growth dynamics, location of muscle attachments, encephalization, or basicranial flexion.

Published by Elsevier Ltd.

Introduction

Pneumatization is the process by which the epithelium infiltrates developing bone, resulting in epithelial-lined air cell tracts within bone. Temporal bone pneumatization is variable across primates (Fig. 1), ranging from a monocellular tympanic bulla in lemurs to the ubiquitous but highly variable patterns of pneumatization documented in humans (Himalstein, 1959). Pneumatized spaces are integral to the structure of the hominid temporal bone, which, because of its density, is commonly recovered paleontologically and, therefore, frequently used in phylogenetic analyses (Weidenreich, 1948; Kimbel et al., 1985; Martinez and Arsuaga, 1997; Lockwood et al., 2002; Vekua et al., 2002; Harvati, 2003; Lockwood et al., 2004). Patterns of temporal bone pneumatization are used as part of a suite of characters to assign phylogenetic status to fossils (Skelton and McHenry, 1992; Strait et al., 1997; Sherwood et al., 2002), and the presence or absence of this trait is commonly reported in fossil specimens (i.e., Kimbel, 1986; Ward et al., 1999; Marquez et al., 2001).

The earliest work on temporal bone pneumatization was completed by Zuckerkandl (1879) but much of the present knowledge on temporal bone pneumatization is derived from extensive clinical research during the last century (Tremble, 1934; Bast and Anson, 1949; Allam, 1969; Shapiro, 1971; Hug and Pfaltz, 1981; Robinson et al., 1993; Sade and Fuchs, 1997; Sade et al., 2006). Much of the early knowledge is based upon either gross anatomical observations (e.g., Diamant, 1940), followed by studies of internal structure using serially sectioned specimens (e.g., Diamant, 1954; Fukuzaki, 1967; Lozupone and Favia, 1990) or radiographs (Schulter-Ellis, 1979; Gregg and Steele, 1982). Advances in medical imaging technology have allowed biologists and clinicians to use computed tomography (CT) scans to observe pneumatization patterns in *Homo* (e.g., Homoe et al., 1992; Luntz et al., 2001), extant nonhuman primate species (Sherwood, 1999), and fossils (Wind, 1984; Balzeau and Grimaud-Hervé, 2006; Balzeau and Radovcic, 2008).

Balzeau and Grimaud-Hervé (2006) and Balzeau and Radovcic (2008). provide the only studies quantifying temporal bone pneumatization in fossils and nonhuman primates to date. Until recently, more extensive analyses have not been possible, given the limitations of imaging technology. Radiographs compress three-dimensional objects into two-dimensional space, thus obscuring the complexity of pneumatization patterns and limiting analyses to calculations of surface areas. Medical resolution CT scans (with slice thicknesses and/or pixel sizes $\geq$0.5 mm) provide data that are

* Corresponding author.
E-mail address: cah1999@gmail.com (C.A. Hill).

0047-2484/$ – see front matter Published by Elsevier Ltd.
doi:10.1016/j.jhevol.2008.03.010

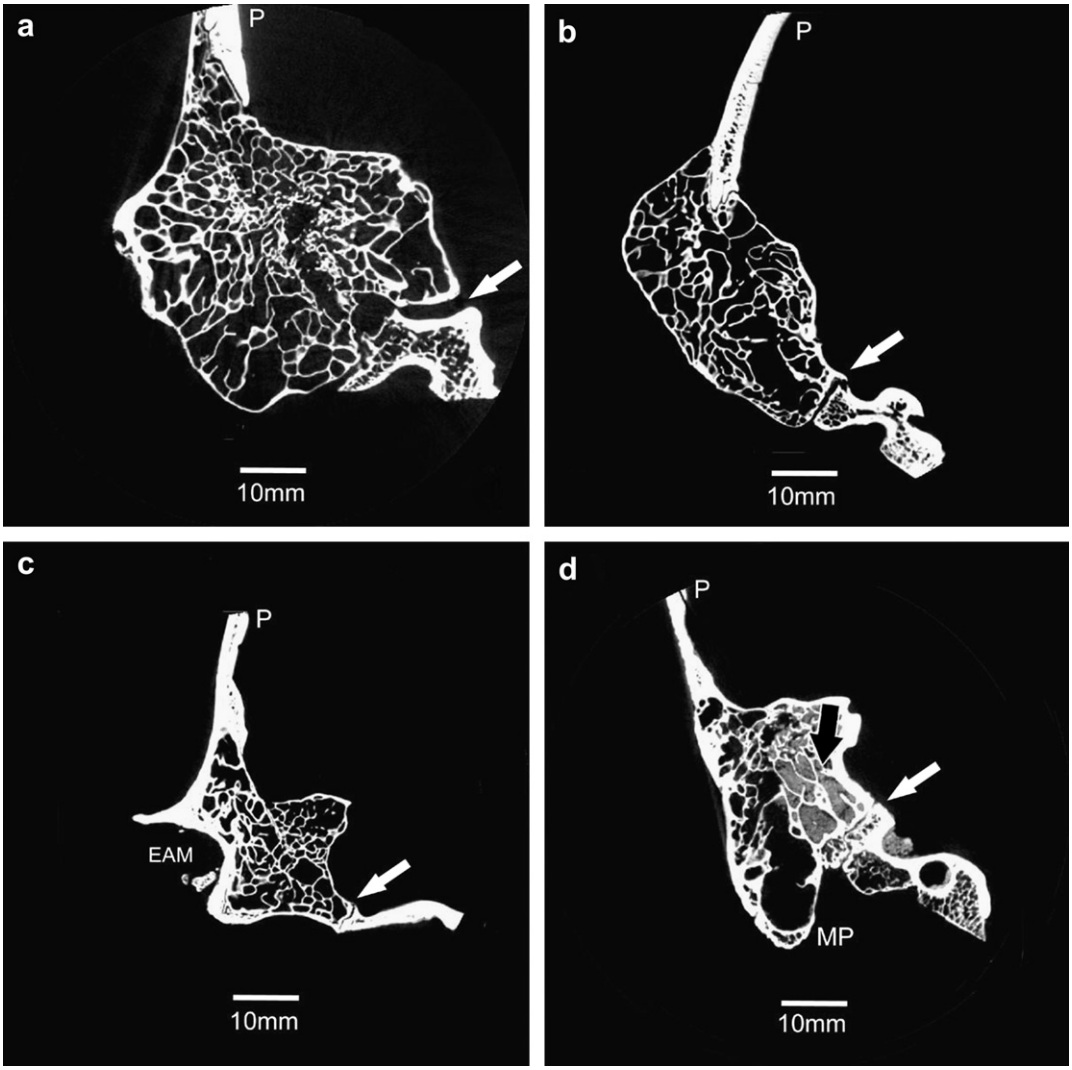

Fig. 1. Cross-sectional slices representing the male mastoid region showing pneumatization in a) *Gorilla*, b) *Pan*, c) *Papio*, and d) *Homo*. These slices are from the posterior view, with the lateral edge of the mastoid region to the left. *Gorilla*, *Pan*, and *Papio* specimens are extensively pneumatized with the air cell tract extending into the squamous portion as well as the mastoid and petrous portions. *Pan* specimens also have pneumatized zygomatic processes. Pneumatization is not as extensive in *Homo* specimens—the air cell tract does not infiltrate the squamous and zygomatic portions. Sediment is evident in the *Homo* specimen (black arrow). White arrows: occipitomastoid suture; (P) parietal; (EAM) external auditory meatus; (MP) mastoid process.

adequate for estimating volume or surface area of air cell tracts, especially in clinical and live animal subjects, but these measures provide limited information beyond overall size for understanding the process of pneumatization and its effect on bone.

Methods developed to maximize the information contained within images of pneumatized spaces acquired by previous imaging modalities demonstrated the usefulness of the study of pneumatization in primate phylogeny and provided a valid foundation for further analyses. Here we introduce an application of novel quantitative methods to the analysis of pneumatized spaces imaged by high-resolution X-ray computed tomography (HRXCT). The methods we apply are adapted from the quantitative analysis of trabecular bone structure.

Materials and methods

Thirty temporal bones from four species were selected for analysis (Table 1). These species were selected for their availability and relevance to analyses of evolutionary change in pneumatization patterns of the hominid temporal bone with *Papio* specimens representing both a morphological and evolutionary outgroup. Skeletal specimens were obtained from the National Museum of Natural History (*Gorilla*), the American Museum of Natural History (*Gorilla, Pan*), the Norris Farms #36 archaeological collection housed at the Pennsylvania State University Department of Anthropology (*Homo*), and the Southwest Foundation for Biomedical Research (SFBR; *Papio*). Nonhuman primate specimens from the National Museum of Natural History and the American Museum of Natural History are wild shot, while *Papio* specimens are captive-bred animals from SFBR. Most specimens from SFBR are necropsied, but careful selection of specimens ensured that the air cell system was intact in the specimens used in this study. The Norris Farms collection (*Homo*) contains modern human skeletons excavated by the Illinois State Museum from a site associated with the Oneota cultural tradition dating to approximately 1300 AD (Milner and Smith, 1990). Adult specimen ages were based on previously recorded museum estimates, and eruption and wear of the third molars. Sex of the specimens was known for *Papio*, but was determined using standard osteological procedures (i.e., pelvic traits), supplemented by museum information where available for the other species. Details of the sex distribution within each species are given in Table 1. Specimens with minimal damage to the

Table 1
Species, sample sizes, and volume dimensions for the specimens used in the current study

Species	Sample (*n*)		Source		Voxel size (mm)		Number of slices	VOI diameter (mm)
	M	F			X, Y	Z		
Papio	2	4	SFBR	*min*	0.061	0.067	656	6.70
				max	0.069	0.077	779	8.54
Gorilla	4	4	NMNH	*min*	0.078	0.087	820	12.81
			AMNH	*max*	0.105	0.122	1189	22.90
Pan	4	4	AMNH	*min*	0.063	0.070	861	8.30
				max	0.075	0.088	1066	11.65
Homo	4	4	Norris	*min*	0.062	0.069	697	8.53
			Farms	*max*	0.078	0.087	984	10.54

temporal bone and little or no breakage or exposure of the pneumatized regions were selected for scanning.

Scanning and image processing

The right or left temporal bone of all specimens were scanned at the Center for Quantitative Imaging at the Pennsylvania State University (www.cqi.psu.edu) using the OMNI-X HD-600 industrial X-ray computed tomography system (Bio-Imaging Research, Inc., Lincolnshire, IL). The system is physically calibrated before each scanning session using a series of phantoms to ensure dimensional integrity of all data and to guarantee appropriate configuration of the system for specific scanning tasks. Calibration includes ensuring appropriate focus and spot size of the X-ray using a wire phantom, calculating vertical distortion, horizontal pitch, and vertical pitch of the detector, determining the center of rotation at numerous vertical positions spanning the range of the scanned object, and generating a wedge table for image processing. Next, the dimensional accuracy is checked using a known-diameter phantom constructed of a material corresponding to the density of the object to be scanned.

To achieve the preferred image resolutions, only one side could be scanned at a time and budget restrictions precluded scanning both left and right sides for each specimen. The skulls were mounted upside-down on florist foam and stabilized with tape during the scanning process. Specimens were scanned with X-ray source energy settings between 150 and 170 kV and between 120 and 200 μA, with 2,400 views and two samples per view. The highest possible resolution relative to skull size was obtained for each specimen so that slice thicknesses and pixel dimensions are largest for *Gorilla* and smaller for the other specimens. Slice thicknesses (Z dimension) ranged from 0.067 to 0.122 mm, depending upon the size of the specimen. The field of view ranged from 62 to 107.52, producing pixel sizes (X and Y dimensions) ranging from 0.0605 to 0.105 mm. Only one scan of a specimen (female gorilla) had voxel dimensions larger than 0.1 mm. The remaining voxel dimensions were less than 0.099 mm^3 for all specimens. Table 1 summarizes image parameters for each taxon.

Serial cross-sectional scans were acquired in the coronal plane for the entire temporal bone of each specimen starting at the occipitomastoid suture and ending at the coronal suture, ensuring capture of the entire petrous portion. Since pneumatized air cell tracts of the human temporal bone do not cross sutural boundaries except in rare clinical disorders (Rebol et al., 2004), all potential pneumatized spaces of the temporal bone were included in the scan volume. This selection produced volumes containing 656 to 1,189 slices per temporal bone depending on the size of each temporal bone. The original 1,024 × 1,024 16-bit TIFF images were reduced to 8-bit images for analysis using ImageJ (National Institutes of Health, available online at: http://rsb.info.nigh.gov/ij/).

Thresholds, which are the values that enable the viewer to visually separate bone (usually visualized in white) from air (visualized as black) in the scan volume, were identified using Quant3D (available online at: http://www.ctlab.geo.utexas.edu/software/), a structural analysis program. A number of methods for determining appropriate thresholds for bone are available for 3D volumes. We selected the iterative method (Ridler and Calvard, 1978; Trussell, 1979) because previous studies indicate that this method is reliable, less laborious, and less error-prone than other methods (e.g., Leung and Lam, 1996; Ryan and Ketcham, 2002a). Threshold selection is crucial to our analyses since the methods adopted here rely on individual voxels for estimating parameters. Incorrect threshold selections will lead to errors in estimation of the proportion of bone to nonbone in the volume (Fig. 2). Unlike medical scans with larger voxel dimensions, HRXCT scans show more averaging within individual voxels leading to blurred air-bone boundaries (Fig. 2). In several archeologically-recovered human specimens, sediment infiltrated the air cells within the

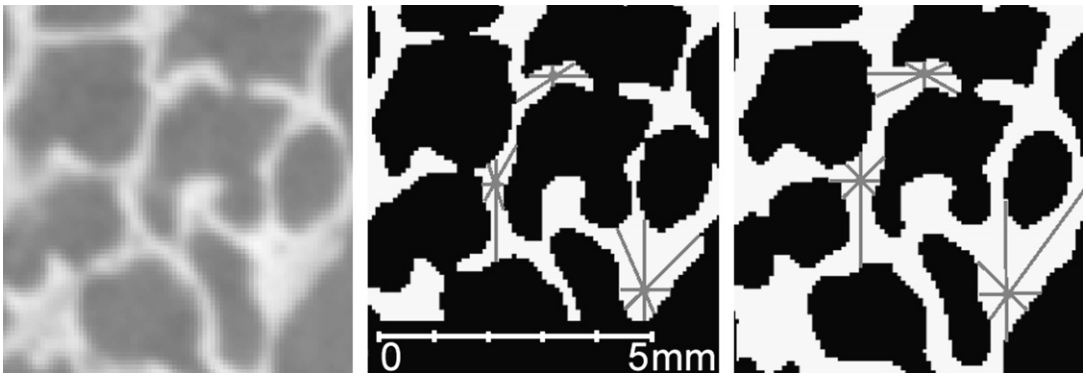

Fig. 2. Selection of the correct threshold is important to prevent the incorrect estimation of the parameters used in this study: (left) original scan data; (middle) overestimated threshold; (right) underestimated low threshold. The SVD method places 8,000 points (gray dots) within the VOI. From these points 2,049 random orientations are drawn between the point and the nearest interface between bone and air (gray lines). If the threshold is too high or low, the amount of bone will be estimated incorrectly.

temporal bone (e.g., Fig. 1d) requiring examination of the computer-generated threshold to ensure that the threshold adequately discriminated between bone and sediment. When necessary, these thresholds were manually adjusted.

A cube-shaped volume surrounding the centroid of the mastoid process was selected from whole temporal bones using Amira 3.1 (available online at: http://www.amiravis.com/). This cube-shaped region of interest (ROI) was oriented coronally (parallel to slice orientation) and defined according to the following anatomical guidelines. The ROI included bone lying along the AP axis from the most posterior edge of the external auditory meatus to the most posterior edge of the petrous temporal where it intersects with the squamous temporal and mastoid near the groove for the sigmoid sulcus. Along the mediolateral axis, the ROI included the most lateral edge of the cortical bone of the mastoid region and continued to the most lateral edge of the semicircular canals. Along the superior-inferior axis, the ROI extended from the superiormost portion of the arcuate eminence to the most inferior edge of the mastoid (Fig. 3). Each ROI was saved as a series of TIFF images. These ROI encompassed nonpneumatized bone including vascular and sensory structures and so were further cropped in Quant3D to include only pneumatized bone. Since previous analyses indicate that nonspherical selections can lead to overestimation of parameters (Ketcham and Ryan, 2004), a spherical volume of interest (VOI) was place within the ROI so that they shared centroids (i.e., the intersection of X, Y, and Z planes). The largest possible VOI was placed in each cropped ROI portion, so that the VOI did not include any non-pneumatized bone, such as cortical bone, trabecular bone, or vascular and sensory structures. The diameter of the VOIs ranged from 6.7 to 22.95 mm (Table 1). For our purposes, we chose corresponding ROIs based on common properties of temporal bone morphology, sutural boundaries, and geometric properties. For all specimens, the VOIs did not include the mastoid antrum or non-pneumatized bone. This systematic protocol for selecting ROIs and VOIs results in the collection of data from corresponding anatomical regions but does not necessarily represent homologous structures.

Previous studies have demonstrated a lack of significant allometric relationships between body size and aspects of trabecular structure, including trabecular thickness (Swartz et al., 1998; Fajardo and Muller, 2001; Parsons et al., 2007). The largest VOI *relative* to the size of the specimen was cropped from the entire temporal bone. *Gorilla* had absolutely larger VOIs, but these VOIs sampled relatively similar spaces compared to other species. The range of sizes among VOIs means that smaller specimens have higher density of sampling points within the VOI compared to larger specimens.

Quantitative analyses

To quantify the morphology of pneumatized spaces in the temporal bone, previously established methods from the trabecular

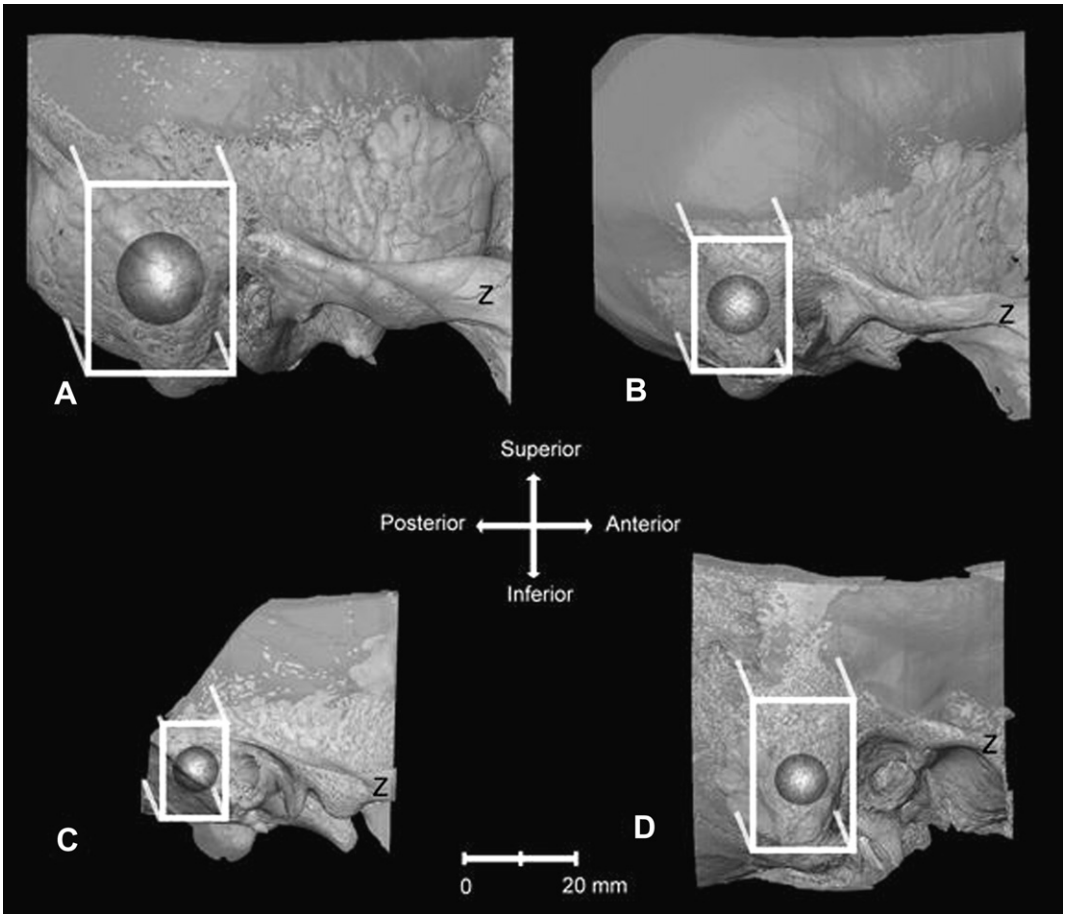

Fig. 3. Transparent three-dimensional reconstructions from HRXCT scans of (A) *Gorilla*, (B) *Pan*, (C) *Papio*, and (D) *Homo* temporal bones showing the mastoid air cell tract and trabecular bone, viewed from the lateral side (Z: zygomatic process). These representations show the selected regions of interest (white box) extending from the edge of the external auditory meatus to the edge of the expansion of the mastoid air cell tract. Since the selected regions of interest included cortical bone, sensory, and vascular structures, the point where orthogonal X, Y, and Z planes intersect in the center of the ROI was selected as the center of the VOI (dark gray sphere). The largest possible VOI was placed within the center of the cropped ROI representing the mastoid region. These VOIs were used to calculate the select parameters in Quant3D. Amira software was used to make the 3D reconstructions.

bone literature were adapted to analysis of the three-dimensional properties of pneumatized bone. Adoption of these methods for the analysis of pneumatized spaces is based on the demonstration of gross similarities in organization of trabecular bone and pneumatized portions of the mastoid process (Lozupone and Favia, 1990). The following measures were selected to describe pneumatized mastoid VOIs: bone volume fractions (BV/TV), trabecular thickness, and anisotropy. Bone volume fractions and trabecular thickness serve as a measure of the amount of bone within the pneumatized regions. BV/TV indicates the proportion of bone volume (BV) to total volume (TV) of the VOI, while trabecular thickness indicates the average thickness of the bony struts within the VOI. Measures of anisotropy reflect directionality of the bone deposition within these spaces. Anisotropy refers to materials that have varying properties that differ according to the direction of measurement. For trabecular bone analyses, anisotropy defines the degree of nonrandom orientation of the trabeculae (Odgaard, 1997; Odgaard et al., 1997) and so by extension could indicate biomechanical demands upon bone during the pneumatization process, or ordered spatial patterns of bone.

Quant3D software was used to estimate bone volume fractions, trabecular thickness, and anisotropy in three-dimensions for each specimen (Ryan and Ketcham, 2002a,b; Ketcham and Ryan, 2004). By using Quant3D, quantification of these three-dimensional parameters in all specimens is straightforward, objective, and automated. Bone volume fractions were estimated for each VOI separately as the ratio of voxels containing bone to the total number of voxels in the VOI. Trabecular thickness and anisotropy are calculated using the star volume distribution method (SVD) that describes the distribution of bone around a typical point in the chosen volume of interest (Cruz-Orive et al., 1992). In our study, 8,000 points are randomly placed on voxels defined as representing bone within the VOI, and intercept lengths are measured for 2,049 orientations in three-dimensional space from each of these 8,000 points to the nearest bone-air interface (Fig. 2). For each orientation, the intercept lengths are recorded as the longest lines lying completely within the bone without intersecting any bone-air interface. Trabecular thickness is measured as the shortest measured intercept lying within the bone phase for each of the 2,049 orientations measured from the 8,000 points placed within each VOI. These intercepts are averaged across the volume of interest to provide an estimate of the size of the bony struts within the volume.

Anisotropy is calculated by compiling the intercept and orientation data into a 3×3 matrix that describes the three-dimensional distribution of the bone within the volume. The eigenvectors ($\hat{u}_1$, $\hat{u}_2$, $\hat{u}_3$) and eigenvalues ($\hat{\tau}_1$, $\hat{\tau}_2$, $\hat{\tau}_3$) from this matrix provide information about orientation and magnitude of the three major axes of the bony material within the VOI. The degree of anisotropy (DA) quantifies the shape of bony struts within the VOI and is calculated by dividing the first eigenvalue by the third eigenvalue ($\hat{\tau}_1/\hat{\tau}_3$). A DA value of 1.0 indicates that intercept lengths within the VOI are similar across dimensions and that the struts are isotropic. DA values not equal to 1.0 indicate dissimilarity in intercept length at any point and suggest that the distribution of the material is anisotropic.

To further describe the shape of the bony struts, additional indices are calculated using the eigenvalues derived from the orientation matrix. The isotropy ($\hat{\tau}_3/\hat{\tau}_1$) and elongation ($1 - \hat{\tau}_2/\hat{\tau}_1$) indices indicate whether the material has plate-like or rod-like structure. A visual display of the isotropy and elongation indices clarifies their relationship and summarizes the relative position of each sample within a triangular plot with vertices that define structures that are completely isotropic, anisotropic rods, and anisotropic plates (Fig. 3; Benn, 1994). Shapes represented at the vertices are extreme so that most specimens will show values that lie somewhere along the continuum between the vertices. For example, a specimen with low isotropy index and high elongation index will fall near the right corner of the diagram indicating that the shape of the struts is more rod-like. Detailed descriptions of the SVD method and anisotropy calculations in Quant3D can be found in Ketcham and Ryan (2004) and Ryan and Ketcham (2002b).

Data provided by Quant3D were analyzed to determine intra- and interspecific differences in pneumatization patterns. Since tests for normality indicated the data were not normally distributed, nonparametric statistical tests were used. Pilot work on image resolution as discussed below indicated that data collected from scans with voxel dimensions >0.100 mm might have elevated observer error. Consequently, the single specimen (*Gorilla*) with scan resolution >0.100 mm was excluded from statistical analyses. Species were compared using Kruskal-Wallis tests and Mann-Whitney U-tests were used to conduct pairwise species comparisons. All statistical analyses were completed with SPSS 15.0 for Windows (SPSS Inc., 2006).

Image resolution, precision, and repeatability

The use of HRXCT presents the researcher with volumes of data and various issues that must be resolved prior to practical implementation of estimated parameters in standard research protocols. In this section, we address two of these issues providing observations and guidelines for other users wanting to make use of HRXCT data. First, we investigate the impact of image resolution on the measured parameters. This discussion addresses the precision of the machine that acquires the HRXCT. Second, we address two issues related to user-induced measurement error: precision and repeatability. We define precision as the average difference between repeated measures on an image of a single individual, while repeatability is the precision of measurement relative to the differences among the images of the individuals in a study (Richtsmeier et al., 1995).

Image resolution. Ideally, the impact of image resolution (i.e., pixel size and slice thickness) on the chosen parameters would be assessed by acquiring both low-resolution CT and HRXCT images of the same specimen and directly comparing parameters estimated using both types of scans. Unfortunately, this approach is cost prohibitive. As an alternative, surrogates for lower resolution scans were created by artificially degrading high-resolution scans to lower resolutions (Muller et al., 1996; Kothari et al., 1998). Three high-resolution VOIs were artificially degraded four times, each time to a larger voxel size (Table 2). The three VOIs were systematically degraded first to the largest voxel sizes used in this study ($\approx$ 0.082/0.091 and 0.105/0.122 voxel dimensions) by resampling the data in Amira. The VOIs were then further degraded to resolutions approximating those used in other analyses of pneumatization (e.g., 0.2/0.24 mm and 0.4/0.48 mm pixel sizes/slice thicknesses). These degradations are an order of magnitude different than those that separate the images acquired for this study but are characteristic of the differences between our images and those used in other pneumatization studies. Quant3D was used to estimate all relevant parameters from the original and degraded datasets, and bone volume fractions, trabecular thickness, and anisotropy values were compared between low- and high-resolution VOIs. Results indicate that the quantified parameters are resolution dependent: the resulting measures differed as resolution decreased. Bone volume fractions and trabecular thicknesses systematically increased as resolution decreased for each VOI. Anisotropy measures also initially increased as resolution decreased, but then decreased at the lowest resolutions. Regardless of these systematic biases, the noted increases in measures between the highest resolution VOI and degradations to slightly

Table 2
Results from pilot work investigating the influence of image resolution. Each scan was artificially degraded four times from the original resolution (first line in bold for each specimen). Once the images were degraded, bone volume fractions (BV/TV), anisotropy (DA), and trabecular thickness (Tb.Th) were calculated for each image resolution

	Resolution (mm)	BV/TV	DA	Tb.Th
Homo	**0.062/0.070**	**0.35**	**2.12**	**0.35**
	0.082/0.091	0.40	2.24	0.39
	0.105/0.122	0.42	2.20	0.41
	0.200/0.240	0.48	2.15	0.51
	0.400/0.480	0.60	1.52	0.77
Pan	**0.063/0.071**	**0.35**	**1.49**	**0.30**
	0.082/0.091	0.38	1.71	0.32
	0.105/0.122	0.43	1.73	0.36
	0.200/0.240	0.49	1.86	0.46
	0.400/0.480	0.62	1.53	0.81
Gorilla	**0.078/0.087**	**0.23**	**4.96**	**0.31**
	0.082/0.091	0.28	5.34	0.36
	0.105/0.122	0.29	5.03	0.37
	0.200/0.240	0.33	4.79	0.46
	0.400/0.480	0.44	3.78	0.71

larger voxel dimensions (0.082/0.091 mm) would not change the results presented here, since these results fall within the standard deviations of the results from HRXCT scans.

These comparisons indicate that, as resolution is radically reduced to resolutions commonly used in analyses of pneumatization based on medical CT, bone volume fractions, trabecular thickness, and anisotropy values increase systematically and erroneously. With larger voxel sizes, Quant3D must progressively estimate the continuation of morphology between slices leading to incorrect (and predominantly inflated) estimates of the true values. Although not all investigators have access to high resolution CT scanners, the error involved in the analysis of pneumatization using images with larger voxel sizes is too great to be of value to any scientific inquiry using the analytical methods proposed here. Analyses using lower resolution images (X, Y, Z $\geq$ 0.100 mm) are not encouraged.

Precision and repeatability. Measurement error was estimated for the parameters used in this study by cropping sample VOIs from HRXCT images of four specimens (one *Pan* and three *Homo*). Ten data collection trials that included estimation of bone volume fractions and anisotropy parameters were completed on each VOI with a minimum of 24 hours elapsing between trials. Means and standard deviations were estimated for the ten trials (data not shown). Within the sample of measures taken on each individual, bone volume fractions demonstrate high precision. Measures of trabecular thickness also demonstrate low error. Anisotropy measures demonstrate a moderate degree of error and reduced precision, with standard deviations ranging from to 2.1 to 6.8 percent, corresponding to Ketcham and Ryan's results (2004). Decreased precision of anisotropy is at least in part due to the random placement of points and of intercept orientation in the estimation of this parameter. Although the error for anisotropy is greater than the other parameters, the error recorded is not so great as to affect the determination of isotropy versus anisotropy and so would not impact the interpretation of our results.

Given the lack of meaningful measurement error in the parameters estimated in Quant3D, an important source of potential error is the selection and placement of the ROIs and VOIs. To test for intraobserver error in placing ROIs and VOIs, four collection trials were completed on six specimens (four *Homo*, one *Pan*, one *Papio*). At 24-hour intervals, ROIs and VOIs were cropped from the larger scan volumes following our defined protocol. These data were analyzed in Quant3D. Means and standard deviations for BV/TV, anisotropy, and trabecular thickness indicate very similar results for BV/TV and trabecular thickness for all trials and specimens (Online Supplementary Materials 1). Anisotropy results demonstrate increased standard deviations matching replication studies by Ketcham and Ryan (2004). Similar to the 10 data collection trials on the same VOI, the variation in anisotropy results would not affect interpretation of isotropy versus anisotropy. Our tests also indicate a significant learning curve, suggesting that measurement error can be reduced over time as experience with the images and the software accumulates. Most importantly, the parameters used in analysis can be estimated from a sample with an acceptable degree of error as long as explicit and precise definitions of ROI/VOI locations are determined.

Results

Bone volume fractions

Descriptive statistics for each species analyzed in this study are listed in Table 3. Individual measures for all parameters are provided in the supplementary material. Pairwise comparisons for sexual dimorphism were completed using Wilcoxon signed rank tests. Results indicate a lack of significant sexual dimorphism in all four species for the parameters quantified in this study ($p \leq 0.05$). Therefore, male and female samples were combined for interspecific statistical comparisons for all parameters. Kruskal-Wallis tests for differences among species in BV/TV values demonstrated significant differences among species ($p = 0.028$). Further testing (Mann-Whitney U-tests) indicates that *Gorilla* has

Table 3
Means and standard deviations (SD) for bone volume fractions (BV/TV), anisotropy (SVD), and trabecular thickness (Tb.Th) in the mastoid process of the specimens included in the statistical analyses. Average image resolution is provided for each sex and species. Results for each individual specimen are provided in Online Supplementary Materials Table 2

Species	Sex	Resolution (mm)		BV/TV		Anisotropy		Tb.Th (mm)	
		X, Y	Z	Mean	SD	Mean	SD	Mean	SD
Papio	M	0.064	0.072	0.31	0.06	1.93	0.29	0.30	0.007
	F	0.061	0.067	0.34	0.08	1.84	0.09	0.29	0.08
	All	0.062	0.068	0.33	0.07	1.87	0.15	0.31	0.07
Gorilla	M	0.082	0.092	0.19	0.02	2.96	1.02	0.41	0.17
	F	0.088	0.100	0.22	0.04	3.09	0.38	0.37	0.12
	All	0.085	0.096	0.20	0.04	3.02	0.76	0.40	0.14
Pan	M	0.070	0.079	0.29	0.09	1.80	0.25	0.28	0.03
	F	0.068	0.078	0.23	0.06	1.87	0.23	0.27	0.03
	All	0.069	0.079	0.26	0.07	1.84	0.22	0.27	0.03
Homo	M	0.078	0.088	0.31	0.07	2.38	0.39	0.36	0.05
	F	0.070	0.079	0.26	0.05	2.29	0.32	0.34	0.07
	All	0.074	0.083	0.28	0.06	2.33	0.34	0.35	0.06

significantly less bony deposition (BV/TV values) than *Homo, Pan*, and *Papio* (Table 4).

Trabecular thickness

Trabecular thicknesses, measured as the average of intercept lengths within each VOI, were statistically compared between all species. Kruskal-Wallis tests for differences among species were significant ($p = 0.034$). Further testing for differences between pairs of species (Mann-Whitney U-tests) indicated that *Pan* has significantly lower trabecular thickness values than *Homo* (Table 4).

Anisotropy

Tests for anisotropy, a parameter that represents directionality among the bony struts within pneumatized spaces, indicate interspecies differences. Kruskal-Wallis tests indicate that the degree of anisotropy ($p = 0.001$), degree of isotropy ($p = 0.001$), and elongation indices ($p = 0.002$) differ significantly among species. Mann-Whitney U-tests were completed to determine which pairs of species demonstrated significant differences in these measures. *Gorilla* has significantly greater anisotropy than *Pan, Papio*, and *Homo,* indicating a stronger tendency for the bony struts in pneumatized spaces to be oriented along a major axis in *Gorilla*. *Homo* has significantly greater anisotropy than *Pan* and *Papio* (Table 4). Differences in anisotropy did not reach statistical significance in the *Pan-Papio* comparison. For most interspecific comparisons, differences in isotropy and elongation indices were significantly different (Table 4). However, the *Pan-Papio* comparison did not show significant differences in these indices.

Indices of anisotropy, isotropy, and elongation are plotted for each individual in Fig. 4. *Pan* exhibits the most isotropic pattern of bony material within the temporal bone, with a mixture of rod-like and plate-like material. For the most part, *Gorilla* demonstrates rod-like shape of the bony material within the VOI. *Papio* have the least variation in material shape, with all individuals tending towards isotropy, and having a equal mixture of rod-like and plate-like structures within the VOI. Analysis of *Homo* reveals a relatively mixed pattern of rod-like, plate-like, and isotropic elements. Figure 4 verifies the statistical similarity in fabric shape among *Pan* and *Papio* on the one hand and *Gorilla* and *Homo* on the other, as well as the significant differences among these species.

Effects of image resolution

Bone volume fractions, anisotropy and trabecular thickness plotted against slice thickness (Fig. 5) suggest that bone volume fractions and anisotropy do not change in relation to increasing slice thickness. Regression analyses show that trabecular thickness has a significant relationship with slice thickness ($p = 0.009$).

Table 4
P-values for the Kruskal-Wallis and Mann-Whitney U-tests of bone volume fractions (BV/TV), degree of anisotropy (DA), and trabecular thickness (Tb.Th). Values in bold were significant at $p \leq 0.05$

Comparison	BV/TV	DA	Tb.Th
Kruskal-Wallis (all species)	**0.028**	**0.001**	**0.034**
Gorilla-Homo	**0.012**	**0.016**	0.743
Gorilla-Pan	**0.027**	**0.014**	0.059
Gorilla-Papio	**0.005**	**0.014**	0.295
Homo-Pan	0.673	**0.002**	**0.011**
Homo-Papio	0.328	**0.008**	0.181
Pan-Papio	0.181	0.950	0.282
Gorilla-Papio[a]	**0.012**	**0.042**	0.648

[a] The results of Mann-Whitney U-tests between *Gorilla* and resampled *Papio* VOIs.

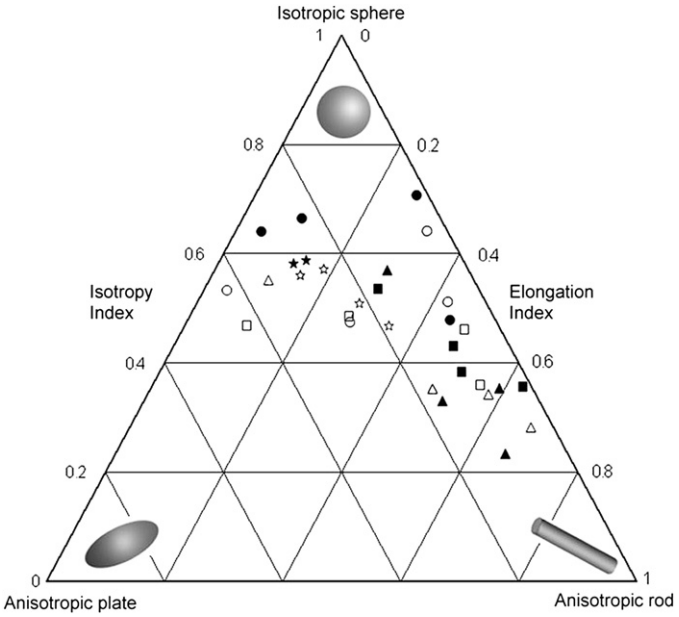

Fig. 4. A ternary diagram plotting the isotropy and elongation indices for each individual in the sample. The relationship between these indices for each specimen provides information about the shape of the structures within the VOI. Isotropic structures cluster near the top, having high isotropy indices and low elongation indices (the degree of anisotropy will be 1.0). At the other extremes, bony deposits can have more plate-like (lower left) or rod-like structure (lower right). ■ male Homo, □ female *Homo,* ▲ male *Gorilla,* △ female *Gorilla,* ● male *Pan*, ○ female *Pan*, ★ male *Papio*, ☆female *Papio.*

However, when *Gorilla* are removed from regression analyses the association is no longer significant ($p = 0.082$).

To further investigate the suspected association between the measured parameters and slice thickness, *Papio* specimens were degraded to the average *Gorilla* resolution. Quant3D analyses were completed using the resampled data. Mann-Whitney U-tests indicated that those comparisons that are significantly different in the original *Papio-Gorilla* comparisons are also signficantly different in the resampled *Papio-Gorilla* comparisons (Table 4). Although this test does not completely address the issue of resolution dependency, it demonstrates that in our analyses of these samples resolution does not account for the differences in the measured parameters. We suggest that future studies of specimens varying greatly in size include resampling of image data so Quant3D data are collected from images of the same resolution.

Discussion and conclusions

The methods presented here have great potential for quantitative description of the three-dimensional morphology of pneumatized spaces and for investigation of species specific or age-dependent differences in patterns of pneumatization. Adoption of methods from the trabecular bone literature (specifically Quant3D) and the use of HRXCT scans allow quantification of the differences, and with proper sample sizes, variation in pneumatization between individuals, sexes and taxa. Additionally, these methods will enable examination of evolutionary and ontogenetic change in the temporal bone.

As HRXCT scanning becomes less expensive, more automated, and less labor-intensive, an increasing number of images will be acquired and made available for extant and fossil species, allowing researchers to analyze pneumatization across larger and more diverse samples. Applying these methods to fossil material will present additional challenges, such as selection of thresholds required to separate fossilized matrix filling pneumatized spaces

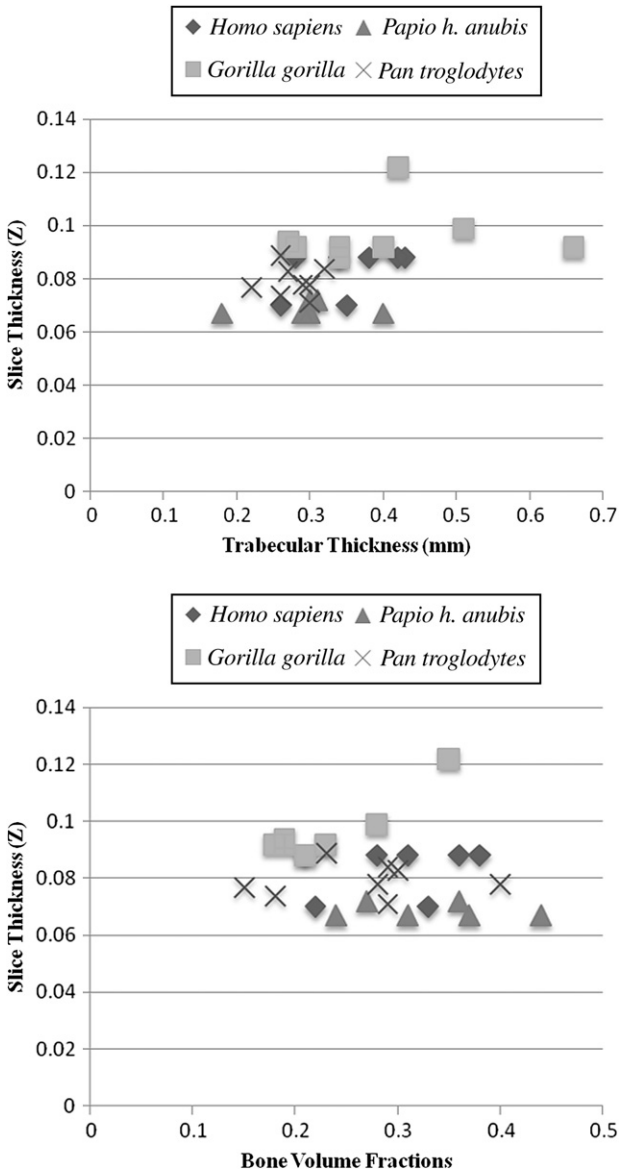

Fig. 5. Graphs plotting trabecular thickness (top) and bone volume fractions (bottom) against slice thickness. Bone volume fractions ($r = 0.191$, $p = 0.312$) and anisotropy (data not shown; $r = 0.337$, $p = 0.068$) do not significantly increase with larger slice thicknesses. Regression analyses indicate that trabecular thickness significantly increases with slice thickness ($r = 0.468$, $p = 0.009$). Removal of *Gorilla* from the regression shows that the association is no longer significant ($r = 0.379$, $p = 0.082$).

from fossilized bone. However, since computed tomography has been used to reconstruct paleontological specimens fully embedded in fossilized matrix (Fraser et al., 2007) we see no reason why this will not be possible. Taphonomic forces resulting in distortion and breakage of bony struts may limit sampling of the mastoid and other pneumatized regions. Still the methods hold promise for analysis of extant and fossil mammalian species and can be used in the analysis of additional regions of the skull.

Although the primary purpose of this paper is to present a novel approach to the study of pneumatization and pneumatized spaces, we have also produced some valuable and intriguing results. Witmer's (1997) epithelial hypothesis states that pneumatized spaces result from epithelium opportunistically expanding into the available space. According to this hypothesis, the size and shape of pneumatized spaces results from two opposing forces: 1) the propensity for epithelium to opportunistically expand, and 2) the need for structurally sound and functionally efficient osseous configuration. Witmer (1997) argues that the nonrandom organization of bony struts within pneumatized spaces provides evidence for the epithelial hypothesis. Consequently, species differences in the requirements of skeletal anatomy should be represented in the organization of pneumaticized spaces. The study presented here was not designed to specifically test this hypothesis, but our analysis provides provisional support for Witmer's hypothesis, as did work by Sherwood (1999). The number of interspecific differences noted may reflect Witmer's idea that pneumatized spaces are the result of continual conflict between bony deposition and epithelial expansion, possibly reflecting interspecific differences in cranial growth patterns or biomechanical requirements of the mastoid region. Bone volume fractions and trabecular bone thicknesses were significantly different among species (Table 4). Anisotropy, which measures the degree of nonrandom orientation of bony material, was also significantly different among species. *Gorilla* has the least amount of bone in the mastoid VOI, but this bone is organized into thicker and more anisotropic struts than in the other species. *Homo*, *Pan*, and *Papio* have similar amounts of bone within the VOI, but this bone is less patterned in *Homo* compared to the other species. The lack of differences between *Pan* and *Papio* may represent a general similarity in ontogeny of mastoid pneumatization or local biomechanical loads between the two species, while the significant differences between *Homo* and *Gorilla* may be influenced by increased encephalization in *Homo* (e.g., Sherwood, 1995, 1999) or other as-yet unidentified factors. These ideas can only serve as guiding hypotheses at this time since this study analyzed an admittedly small number of specimens from only four primate species. Ongoing research has already shown that increasing sample sizes can change statistical outcomes and consequent interpretations of patterns of interspecific differences in temporal bone pneumatization (Hill, 2008).

Ongoing research, including acquisition of larger samples of micro-computed tomographic images and more extensive sampling from other pneumatized spaces, including the entire mastoid process, petrous apex, squamous, and zygomatic portions, will provide new information pertaining to the development and significance of these enigmatic structures. The quantitative methods presented here can be directly applied in quantitative analysis of pneumatization patterns for objective use in phylogenetic analysis. In addition, these methods may prove useful in elucidation of the biological mechanisms that underlie pneumatization providing an explanation for evolutionary and developmental change in the pneumatized spaces.

Acknowledgments

Online supplementary materials are available at www.getahead.psu.edu and in the online version of this article. This paper was much improved by comments provided by two anonymous reviewers and the associate editor. We thank the curators of the National Museum of Natural History, the American Museum of Natural History, the Illinois State Museum, and Dr. James Cheverud of Washington University-St Louis and the Southwest Foundation for Biomedical Research for loaning the skeletal material used in this study. We also thank Timothy Ryan for excellent technical support in acquiring the HRXCT images, and critical discussion and assistance with the methods used in this paper. This work was supported by the Pennsylvania State University, the Leakey Foundation, NSF (BCS-052493, BCS-0523637 and PHS (RO1 DE016886, RO1 DE018500).

Appendix. Supplementary materials

Supplementary data associated with this article can be found in the online version at doi:10.1016/j.jhevol.2008.03.010.

References

Allam, A.F., 1969. Pneumatization of the temporal bone. Annls. Otol. Rhinol. Laryngol. 78, 49–64.

Balzeau, A., Grimaud-Hervé, D., 2006. Cranial base morphology and temporal bone pneumatization in Asian *Homo erectus*. J. Hum. Evol. 51, 350–359.

Balzeau, A., Radovcic, J., Variation and modalities of growth and development of the temporal bone pneumatization in Neandertals. J. Hum. Evol. 54, 546–567.

Bast, T.H., Anson, B.J., 1949. The Temporal Bone and the Ear. Charles C Thomas, Springfield.

Benn, D.I., 1994. Fabric shape and the interpretation of sedimentary fabric data. J. Sediment. Res. A64, 910–915.

Cruz-Orive, L.M., Karlsson, L.M., Larsen, S.E., Wainschtein, F., 1992. Characterizing anisotropy: a new concept. Micron Microsc. Acta 23, 75–76.

Diamant, M., 1940. Otitis and Pneumatisation of the Mastoid Bone: A Clinical-Statistical Analysis. H. Ohlsson, Lund.

Diamant, M., 1954. Size variation of the mastoid air cell system according to Wittmaack, Schwarz and Diamant. Acta. Otolaryngol. Suppl. 118, 54–67.

Fajardo, R.J., Muller, R., 2001. Three-dimensional analysis of nonhuman primate trabecular architecture using micro-computed tomography. Am. J. Phys. Anthropol. 115, 327–336.

Fraser, N.C., Olsen, P.E., Dooley, A.C., Ryan, T.R., 2007. A new gliding tetrapod (Diapsida:? Archosauromorpha) from the Upper Triassic (Carnian) of Virginia. J. Vert. Paleontol. 27, 261–265.

Fukuzaki, T., 1967. A histological observation of the development of human mastoid cells. Nippon Jibiinkoka Gakkai Kaiho 70, 1243–1254 (in Japanese).

Gregg, J.B., Steele, J.P., 1982. Mastoid development in ancient and modern populations. A longitudinal radiological study. J. Am. Med. Assoc. 248, 459–464.

Harvati, K., 2003. Quantitative analysis of Neanderthal temporal bone morphology using three-dimensional geometric morphometrics. Am. J. Phys. Anthropol. 120, 323–338.

Himalstein, M.R., 1959. Mastoid pneumatization: a case with interesting developmental and phylogenetic aspects. Trans. Am. Laryngol. Rhinol. Otol. Soc. 1959, 606–615.

Hill, C.A., 2008. Evolution and development of temporal bone pneumatization in hominids. Ph.D. Dissertation, Pennsylvania State University.

Homoe, P., Lynnerup, N., Videbaek, H., 1992. CT-scanning of ancient Greenlandic Inuit temporal bones. Acta. Otolaryngol. 112, 674–679.

Hug, J.E., Pfaltz, C.R., 1981. Temporal bone pneumatization. A planimetric study. Arch. Otorhinolaryngol. 233, 145–156.

Ketcham, R.A., Ryan, T.M., 2004. Quantification and visualization of anisotropy in trabecular bone. J. Microscop. 213, 158–171.

Kimbel, W.H., 1986. Calvarial morphology of *Australopithecus afarensis*: a comparative phylogenetic study. Ph.D. Thesis, Kent State University.

Kimbel, W.H., White, T.D., Johanson, D.C., 1985. Craniodental morphology of the hominids from Hadar and Laetoli: evidence of "*Paranthropus*" and *Homo* in the Mid-Pliocene of eastern Africa. In: Delson, E. (Ed.), Ancestors: The Hard Evidence. Alan R. Liss Inc., New York, pp. 120–137.

Kothari, M., Keaveny, T.M., Lin, J.C., Newitt, D.C., Genant, H.K., Majumdar, S., 1998. Impact of spatial resolution on the prediction of trabecular architecture parameters. Bone 22, 437–443.

Leung, C.K., Lam, F.K., 1996. Performance analysis for a class of iterative image thresholding algorithms. Pattern. Recog. 29, 1523–1530.

Lockwood, C.A., Kimbel, W.H., Lynch, J.M., 2004. Morphometrics and hominoid phylogeny: support for a chimpanzee-human clade and differentiation among great ape subspecies. Proc. Natl. Acad. Sci. U. S. A. 101, 4356–4360.

Lockwood, C.A., Lynch, J.M., Kimbel, W.H., 2002. Quantifying temporal bone morphology of great apes and humans: an approach using geometric morphometrics. J. Anat. 201, 447–464.

Lozupone, E., Favia, A., 1990. The structure of the trabeculae of cancellous bone. 2. Long bones and mastoid. Calcif. Tissue Int. 46, 367–372.

Luntz, M., Malatskey, S., Tan, M., Bar-Meir, E., Ruimi, D., 2001. Volume of mastoid pneumatization: three-dimensional reconstruction with ultrahigh-resolution computed tomography. Annls. Otol. Rhinol. Laryngol. 110, 486–490.

Marquez, S., Mowbray, K., Sawyer, G.J., Jacob, T., Silvers, A., 2001. New fossil hominid calvaria from Indonesia—Sambungmacan 3. Anat. Rec. 262, 344–368.

Martinez, I., Arsuaga, J.L., 1997. The temporal bones from Sima de los Huesos middle Pleistocene site (Sierra de Atapuerca, Spain). A phylogenetic approach. J. Hum. Evol. 33, 283–318.

Milner, G.W., Smith, V.G., 1990. Oneota human skeletal remains. In: Santure, S.K., Harn, A.D., Esarey, D. (Eds.), Archaeological Investigations at the Morton Village and Norris Farms 36 Cemetery. Illinois State Museum, Springfield, pp. 111–148.

Muller, R., Koller, B., Hildebrand, T., Laib, A., Gianolini, S., Ruegsegger, P., 1996. Resolution dependency of microstructural properties of cancellous bone based on three-dimensional m-tomography. Technol. Health Care 4, 113–199.

Odgaard, A., 1997. Three-dimensional methods for quantification of cancellous bone architecture. Bone 20, 315–328.

Odgaard, A., Kabel, J., van Rietbergen, B., Dalstra, M., Huiskes, R., 1997. Fabric and elastic principal directions of cancellous bone are closely related. J. Biomech. 30, 487–495.

Parsons, T., Ryan, T.M., Reeves, R.H., Richtsmeier, J.T., 2007. Microstructure of trabecular bone in a mouse model for Down syndrome. Anat. Rec. (Hoboken) 290, 414–421.

Rebol, J., Munda, A., Tos, M., 2004. Hyperpneumatization of the temporal, occipital, and parietal bones. Eur. Arch. Otorhinolaryngol. 261, 445–448.

Richtsmeier, J.T., Paik, C.H., Elfert, P.C., Cole III, T.M., Dahlman, H.R., 1995. Precision, repeatability, and validation of the localization of cranial landmarks using computed tomography scans. Cleft Palate Craniofac. J. 32, 217–227.

Ridler, T.W., Calvard, S., 1978. Picture thresholding using an iterative selection method. IEEE T. Syst. Man Cyb. 8, 630–632.

Robinson, P.J., Lodge, S., Goligher, J., Bowley, N., Grant, H.R., 1993. Secretory otitis media and mastoid air cell development. Int. J. Pediatr. Otorhinolaryngol. 25, 13–18.

Ryan, T.M., Ketcham, R.A., 2002a. Femoral head trabecular bone structure in two omomyid primates. J. Hum. Evol. 43, 241–263.

Ryan, T.M., Ketcham, R.A., 2002b. The three-dimensional structure of trabecular bone in the femoral head of strepsirrhine primates. J. Hum. Evol. 43, 1–26.

Sade, J., Fuchs, C., 1997. Secretory otitis media in adults 2. The role of mastoid pneumatization as a prognostic factor. Annls. Otol. Rhinol. Laryngol. 106, 37–40.

Sade, J., Russo, E., Fuchs, C., Ar, A., 2006. Acute otitis media and mastoid growth. Acta Otolaryngol. 126, 1036–1039.

Schulter-Ellis, F.P., 1979. Population differences in cellularity of the mastoid process. Acta Otolaryngol. 87, 461–465.

Shapiro, S.L., 1971. The Wittmaak theory of pneumatization. Eye Ear Nose Throat Mon. 50, 312–316.

Sherwood, R.J., 1995. The hominid temporal bone: ontogeny and phylogenetic implications. Ph.D. Dissertation, Kent State University.

Sherwood, R.J., 1999. Pneumatic processes in the temporal bone of chimpanzee (*Pan troglodytes*) and gorilla (*Gorilla gorilla*). J. Morphol. 241, 127–137.

Sherwood, R.J., Ward, S.C., Hill, A., 2002. The taxonomic status of the Chemeron temporal (KNM-BC 1). J. Hum. Evol. 42, 153–184.

Skelton, R.R., McHenry, H.M., 1992. Evolutionary relationships among early hominids. J. Hum. Evol. 23, 309–349.

SPSS Inc, 2006. SPSS for Windows, Rel. 15.0. 2006. SPSS Inc., Chicago.

Strait, D.S., Grine, F.E., Moniz, M.A., 1997. A reappraisal of early hominid phylogeny. J. Hum. Evol. 32, 17–82.

Swartz, S.M., Parker, A., Huo, C., 1998. Theoretical and empirical scaling patterns and topological homology in bone trabeculae. J. Exp. Biol. 201, 573–590.

Tremble, G.E., 1934. Pneumatization of the temporal bone. Arch. Otolaryngol. 19, 172.

Trussell, H.J., 1979. Comments on "picture thresholding using an iterative selection method". IEEE T. Syst. Man Cyb. 9, 311.

Vekua, A., Lordkipanidze, D., Rightmire, G.P., Agusti, J., Ferring, R., Maisuradze, G., Mouskhelishvili, A., Nioradze, M., De Leon, M.P., Tappen, M., Tvalchrelidze, M., Zollikofer, C., 2002. A new skull of early *Homo* from Dmanisi, Georgia. Science 297, 85–89.

Ward, C., Leakey, M., Walker, A., 1999. The new hominid species *Australopithecus anamensis*. J. Hum. Evol. 7, 197–205.

Weidenreich, F., 1948. About the Morphological Character of the Australopthecine Skull. Robert Broom Commemorative Volume, Special Publication of the Royal Society of South Africa. Royal Society of South Africa, Cape Town.

Wind, J., 1984. Computerized X-ray tomography of fossil hominid skulls. Am. J. Phys. Anthropol. 63, 265–282.

Witmer, L.M., 1997. The evolution of the antorbital cavity of archosaurs: a study in soft-tissue reconstruction in the fossil record with an analysis of the function of pneumaticity. J. Vert. Paleontol. 17, 1–75.

Zuckerkandl, E., 1879. Zur Anatomie des Warzenfortsatzes. Monatsschrift fur Ohrenheilkunde 13, 49–54.